Research Article

Hydrothermal synthesis of monodispersed $CePO_4:Tb^{3+}$ porous microspheres and their redox-responsive luminescence

Shuhei Takasu[1] · **Manabu Hagiwara**[1] · **Shinobu Fujihara**[1]

Abstract

Monodispersed $CePO_4:Tb^{3+}$ microspheres, which were formed by aggregation of primary nanoparticles, were synthesized by a hydrothermal reaction method assisted with ethylenediaminetetraacetic acid. The microspheres were found to have a hierarchically porous structure as well as a high specific surface area according to structural and chemical analyses. The microspheres exhibited green photoluminescence (PL) due to 4*f*–4*f* electronic transitions of Tb^{3+} ions doped in the $CePO_4$ crystal upon irradiation with ultraviolet light. The microspheres were then treated with an oxidant (potassium permanganate) and a reductant (L(+)-ascorbic acid) in aqueous solutions at room temperature to examine their effect on the PL property. The PL intensity of the microspheres was once decreased by the oxidation and then increased by the reduction. Such the change in the PL intensity was also shown to be quantitative against the concentration of the oxidant and the reductant. Thus the monodispersed $CePO_4:Tb^{3+}$ porous microspheres were demonstrated to be a facile luminescence-sensing material.

Keywords Phosphor · Luminescence · Particle · Aggregate · Redox reaction · Sensing

1 Introduction

Phosphor powders have long been used in the field of optoelectronics including displays and lighting [1]. Individual particles of phosphor powders should commonly be well crystallized and grown by high temperature treatments and have micrometer dimensions. These characteristics are important for phosphor powders employed in optoelectronic devices which require high luminescence intensities as a whole. That is, thick films or screens consisting of micrometer-sized phosphor particles can exhibit high luminance due to multiple reflection and scattering of both excitation and emission light [2].

Recently, nanometer-sized phosphor particles have attracted much attention because of their many possible applications, such as transparent devices [3], spectral converters [4], solid-state lighting [5], and biomedical imaging [6]. Besides, we have focused on the use of nanophosphors as chemical sensors [7]. Nanometer-sized particles with high specific surface areas are necessary for luminescence sensing of chemical species in various environments. This is because any chemical interaction that can change luminescent properties occurs at the surface of phosphor particles. It was previously demonstrated that $CePO_4:Tb^{3+}$ nanophosphors could exhibit luminescence on/off switching phenomena in response to reduction/oxidation treatments and were thus promising as redox sensors [8, 9]. However, a problem has arisen that the nanophosphors are difficult to handle especially when collecting after the redox treatments in liquid media: they need to be collected by centrifuging and washing after each treatment. Moreover, a small fraction of the nanophosphors is always lost by flowing out throughout each procedure of the redox treatments.

In the present study, we attempted to synthesize $CePO_4:Tb^{3+}$ phosphor powders having a new morphology

✉ Shinobu Fujihara, shinobu@applc.keio.ac.jp | [1]Department of Applied Chemistry, Keio University, 3-14-1 Hiyoshi, Kohoku-ku, Yokohama 223-8522, Japan.

SN Applied Sciences (2019) 1:807 | https://doi.org/10.1007/s42452-019-0854-0

Received: 10 May 2019 / Accepted: 27 June 2019 / Published online: 1 July 2019

of porous microspheres suitable for luminescence sensing. The structure of the microspheres was designed so that they could be handled easily while keeping their high redox sensitivity. A hydrothermal reaction assisted with ethylenediaminetetraacetic acid (EDTA) was introduced to synthesize monodispersed $CePO_4$:Tb^{3+} microspheres comprising of primary nanoparticles. The size uniformity is of great significance to regulate the redox reaction in the respective microspheres. Luminescent properties of the monodispersed microspheres were then examined in association with their redox response.

2 Experimental

2.1 Materials and synthesis

Monodispersed $CePO_4$:Tb^{3+} microspheres were synthesized by the hydrothermal reaction method, as described below. A 2.18 mmol portion of ethylenediaminetetraacetic acid disodium salt dihydrate ($[CH_2N(CH_2COOH)CH_2COONa]_2{\cdot}2H_2O$, EDTA-2Na, Wako Pure Chemical Industries, Ltd., Japan) was dissolved in 10 mL of deionized water. Separately, 0.144 mmol of $Ce(NO_3)_3{\cdot}6H_2O$ (Wako) and 0.576 mmol of $Tb(NO_3)_3{\cdot}6H_2O$ (Wako) were dissolved together in 5 mL of deionized water. The Ce^{3+}/Tb^{3+} solution was then added dropwise to the EDTA solution with simultaneous addition of ammonia water (28%, Wako) to adjust the pH value to 3.5. A 0.960 mmol portion of ammonium dihydrogen phosphate ($NH_4H_2PO_4$, Kanto Chemical Co., Inc., Japan) was dissolved in deionized water, which was further added to the above Ce^{3+}/Tb^{3+}/EDTA solution with the pH value kept around 3.5. The resultant aqueous solution, which was transparent and free from any precipitates, was placed in a Teflon-lined autoclave, preheated to 100 °C, and finally heated at 150 °C for 2 h under a static hydrothermal condition, followed by natural cooling to room temperature. Powder products were collected by suction filtration, washed with deionized water, and dried at room temperature.

2.2 Characterization

The crystal structure of the powder was identified by X-ray diffraction (XRD) analysis using CuKα radiation (λ = 1.5418 Å) with a D8 ADVANCE diffractometer (Bruker, Japan). The elemental analysis of the powder was performed by X-ray fluorescence (XRF) spectroscopy with an XGT-2700 X-ray analytical microscope (Horiba, Japan). The morphology of the powder was observed by field-emission scanning electron microscopy (FESEM) with an Inspect F50 microscope (FEI, USA) and transmission electron microscopy (TEM) with a Tecnai F20 microscope (FEI). Fourier transform infrared (FT-IR) spectra of the powder were measured using the KBr method with an ALPHA spectrophotometer (Bruker). Thermal behavior of the powder was examined in air by thermogravimetry–differential thermal analysis (TG–DTA) with a DTG-60 system (Shimadzu, Japan). The specific surface area of the powder was estimated by the Brunauer–Emmett–Teller (BET) method based on the nitrogen adsorption isotherm at 77 K with a Tristar 3000 Micrometrics analyzer (Shimadzu). An approximately 0.1 g portion of the powder was heated at 160 °C for 4 h under reduced pressure to remove unnecessary adsorbed species before the BET measurement. Photoluminescence (PL) spectra of the powder were measured at room temperature with an FP-6500 spectrofluorophotometer (JASCO, Japan). A filter was used to remove a second-order peak of the excitation light. The powder was mounted on a silica glass plate having a square well 5 mm × 5 mm in dimension to regulate their amount in the PL measurement.

2.3 Redox treatment

The amount of the powder was increased by repeating the above-mentioned synthetic procedure for the examination of the redox responsivity. In one set of experiments, 72 mg of the powder (the as-prepared Powder A) was added to 10 mL of an aqueous $KMnO_4$ solution (0.50 mmol L^{-1}), followed by stirring for 2 h at room temperature. The powder was collected by suction filtration, washed with deionized water, and dried at room temperature to obtain the oxidized Powder O. A 60 mg portion of Powder O was added to 10 mL of an aqueous L(+)-ascorbic acid solution (1.25 mmol L^{-1}), followed by stirring for 2 h at room temperature. The powder was collected similarly to obtain the oxidized/reduced Powder R.

In the other set of experiments, 36 mg of Powder A was added to one of aqueous $KMnO_4$ solutions (5 mL) with concentrations between 0.020 and 0.080 mmol L^{-1}, followed by stirring for 2 h at room temperature. The powder was collected similarly to obtain the oxidized Powder O-x (x = 0.02, 0.04, 0.06, or 0.08 in accordance with the $KMnO_4$ concentrations). Next, a 180 mg portion of Powder A was added to 25 mL of the aqueous $KMnO_4$ solution (0.080 mmol L^{-1}), followed by stirring for 2 h at room temperature. A 36 mg portion of the resultant oxidized powder was added to one of aqueous L(+)-ascorbic acid solutions (5 mL) with concentrations between 0.050 and 0.20 mmol L^{-1}, followed by stirring for 2 h at room temperature. The powder was collected similarly to obtain the oxidized/reduced Powder R-y (y = 0.050, 0.10, 0.15, or 0.20 in accordance with the L(+)-ascorbic acid concentrations).

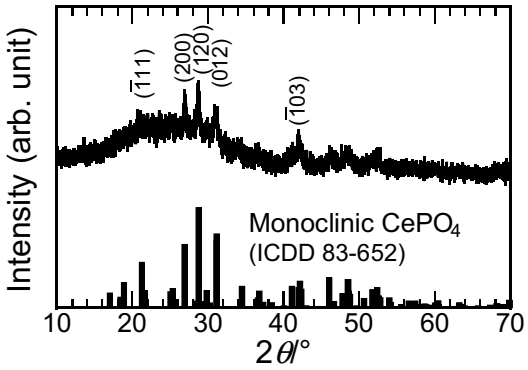

Fig. 1 An XRD pattern of the as-prepared Powder A obtained by the hydrothermal method

3 Results and discussion

3.1 Characterization of $CePO_4$:Tb^{3+} powders

There are at least two kinds of crystal structures in $CePO_4$: the hexagonal rhabdophane-type structure and the monoclinic monazite-type structure [10, 11]. An XRD pattern of the as-prepared Powder A shown in Fig. 1 indicates that it crystallized in the monoclinic system during the hydrothermal treatment at 150 °C. Gulnar et al. [12, 13] also reported the crystallization of the monoclinic $CePO_4$ nanomaterials synthesized at 140 °C in ethylene glycol medium. In our previous works, on the other hand, the nanocrystalline $CePO_4$:Tb^{3+} samples prepared at room temperature by the coprecipitation [8] or the successive ionic layer adsorption and reaction [14] were obtained as the hexagonal system with the unique morphology of nanorods. As shown in Fig. 2, the morphology of Powder A is the aggregation of isometric nanoparticles (approximately 10 nm in size) that form monodispersed secondary particles (microspheres) as large as 800 nm in size. Therefore, both the crystallization and the crystal growth of the $CePO_4$ phase depend on the reaction condition in the synthetic procedure. The rare earth composition in the $CePO_4$ phase was determined to be Ce^{3+}:Tb^{3+} = 0.894:0.106 from the XRF spectroscopy. This composition was obtained from the solution with Ce^{3+}:Tb^{3+} = 0.200:0.800 and had been preliminarily optimized by examining the relationship between the starting composition of the reaction solutions and the final composition of the solid products.

The role of EDTA in the hydrothermal synthesis of $CePO_4$:Tb^{3+} is twofold. Firstly, it stabilizes the Ce^{3+} and Tb^{3+} ions in the aqueous solution and prevent them from the direct precipitation as $CePO_4$:Tb^{3+} when mixing with the $NH_4H_2PO_4$ solution. The stability constant, K, of the complex formed between the rare earth metal ion (designated as M^{3+}) and the anion of ethylenediaminetetraacetic acid (Y^{4-}) is defined as follows.

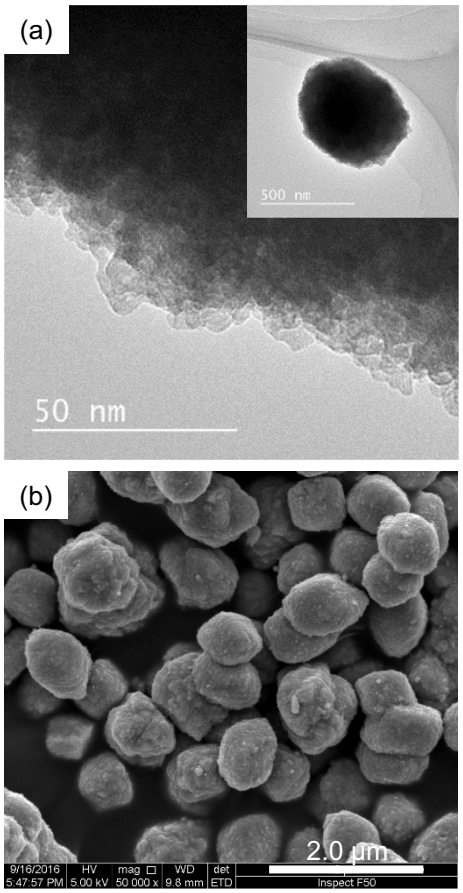

Fig. 2 **a** High and low magnification TEM images and **b** an FESEM image of Powder A

$$K = [MY^{-}]/\left(\left[M^{3+}\right]\left[Y^{4-}\right]\right) \quad (1)$$

The values of log K are reported to be as large as 15.39 for Ce^{3+} and 17.25 for Tb^{3+} [15]. It is also worth mentioning that the higher stability of the Tb^{3+} complex led to the necessity of increasing the Tb^{3+} concentration in the reaction solutions to incorporate Tb^{3+} in the $CePO_4$ phase. That is why the starting composition of Ce^{3+}:Tb^{3+} = 0.200:0.800 employed in the present experiment yielded the final composition of Ce^{3+}:Tb^{3+} = 0.894:0.106 analyzed for the $CePO_4$:Tb^{3+} product.

Secondly, EDTA would be adsorbed on the growing $CePO_4$:Tb^{3+} nanoparticles and regulate the shape of the secondary particles into the monodispersed microspheres during the hydrothermal treatment. Actually, the aggregation is disturbed and the particles are irregularly shaped when the amount of EDTA in the reaction solution is decreased from the present condition. The precise tuning of the size of the monodispersed microspheres will be our next challenge. Figure 3 shows an FT-IR spectrum

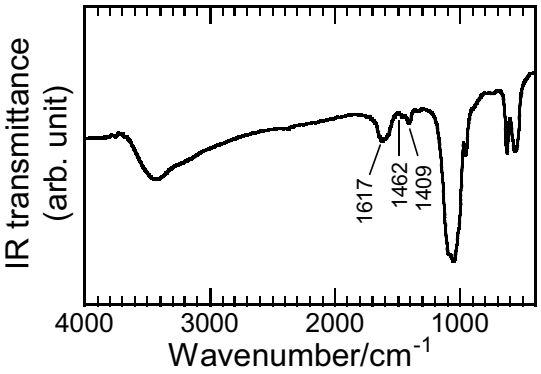

Fig. 3 An FT-IR spectrum of Powder A

of Powder A. Relatively intense absorption bands are observed due to the stretching vibration mode of the hydroxyl group between 3700 and 3300 cm^{-1}, the bending mode of the hydroxyl group around 1620 cm^{-1}, the v_3 stretching mode of PO_4^{3-} around 1060 cm^{-1}, and the v_4 bending mode of PO_4^{3-} between 500 and 700 cm^{-1} [16–18]. There also appear absorption bands due to the antisymmetric (v_{anti}) and the symmetric (v_{sym}) stretching mode of the carboxy group around 1617 and 1409 cm^{-1} [19], respectively, which clearly indicates the presence of EDTA in Powder A. A relatively weak band due to the deformation mode of CH_2 [20] is also detected at 1462 cm^{-1}. The difference (Δv) between the v_{anti} and the v_{sym} frequency can be used to judge the state of the carboxy group [19, 21]. The Δv value of the present study, 208 cm^{-1}, indicates that the carboxylate (COO^-) in EDTA is coordinated to the $CePO_4$:Tb^{3+} nanoparticles in the unidentate form.

Figure 4 shows TG–DTA curves of Powder A. A first weight loss with a small and broad endothermic peak at temperatures up to 100 °C corresponds to the release of water adsorbed onto the nanoparticles. Further weight losses occur in multistep due to the decomposition of EDTA. Such a thermal behavior is characteristic of the rare-earth complexes of EDTA [22]. A continuous decrease in the weight up to a high temperature of 900 °C may be due to the incorporation of EDTA inside the microspheres and its gradual decomposition.

Figure 5a shows an adsorption–desorption isotherm plot for the nitrogen sorption (77 K) of Powder A. The shape of the plot can be interpreted as a combination of a type I and a type IV isotherm [23, 24]. That is, a rapid rise with high adsorbed volumes at low relative pressures (type I) indicates the presence of micropores in the microspheres. In a magnified plot (Fig. 5b), a slight hysteresis is clearly observed at high pressures (type IV), which is due to the presence of meso- and macropores. A rapid increase in the adsorbed volume above the relative pressure of 0.9 is actually attributed to the multilayer adsorption inside the macropores. The BET specific surface area of Powder A was determined to be 51.4 $m^2\ g^{-1}$. This value reflects the relatively higher adsorbed volume in the isotherm plot and is much higher than that expected from the 800-nm sized solid particles (approximately 1.4 $m^2\ g^{-1}$). The microspheres have therefore a hierarchically porous structure, which is expected to provide effective reaction sites for redox species as described later.

PL excitation and emission spectra of Powder A are shown in Fig. 6. The excitation spectrum was measured for the emission wavelength (λ_{em}) of 544 nm and the emission spectrum was monitored with the excitation wavelength (λ_{ex}) of 276 nm. Obviously the emission spectrum consists of four characteristic emission lines, which are ascribed to $^5D_4 \rightarrow {}^7F_6$ (489 nm), $^7F_5$ (544 nm), $^7F_4$ (584 nm), and $^7F_3$ (621 nm) electronic transitions of the Tb^{3+} ion having a $4f^8$ electronic configuration. On the other hand, the broad excitation band is attributed to the optical absorption of the Ce^{3+} ion with $^2F_{5/2}$ ($4f^1$) $\rightarrow {}^2D$ ($5d^1$) electronic transition, followed by energy transfer to the Tb^{3+} ion. These results indicate that the Tb^{3+} ions are successfully incorporated into the $CePO_4$ lattice in hydrothermally derived Powder A.

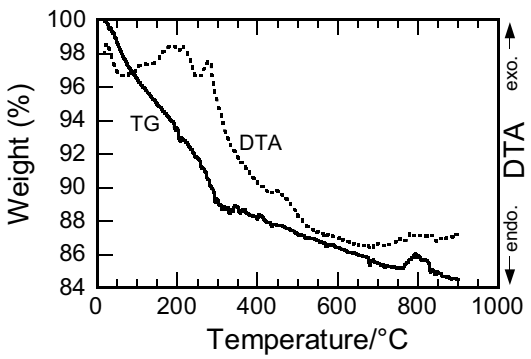

Fig. 4 TG–DTA curves of Powder A

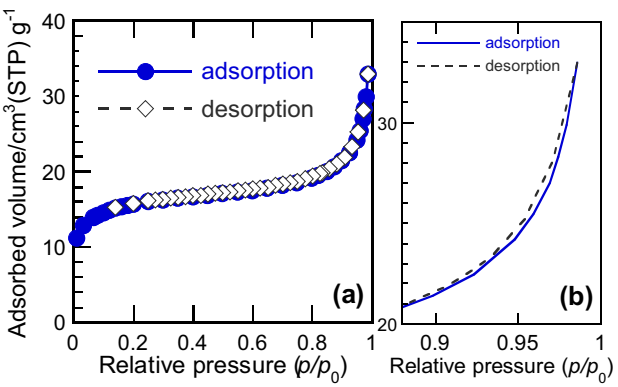

Fig. 5 **a** Full and **b** expanded nitrogen adsorption-desorption isotherms of Powder A at 77 K

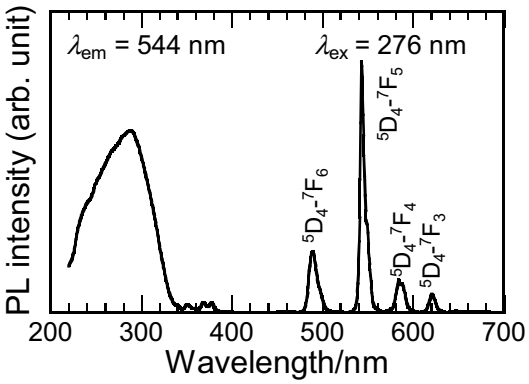

Fig. 6 PL excitation and emission spectra of Powder A

3.2 Redox treatment of monodispersed $CePO_4$:Tb^{3+} microspheres

The redox response of Powder A is described hereafter to evaluate it as a sensing material. Figure 7a compares XRD patterns of Powder A, Powder O that was obtained by oxidizing Powder A, and Powder R that was obtained by reducing Powder O. All the patterns can be identified as the $CePO_4$ phase with the monoclinic monazite-type structure, as discussed with Fig. 1, and hence no XRD-detectable structural change is observable after the redox treatment. The morphology of Powder A, O, and R is shown in Fig. 7b as FESEM images. The 800-nm sized microspheres of Powder A are not destroyed after the oxidation (Powder O) and the reduction (Powder R). Therefore the aggregation is enough strong for the use of the microspheres as redox sensors in the aqueous media.

Figure 8 shows PL excitation and emission spectra of Powder A, O, and R, together with their optical images under the irradiation with an ultraviolet (UV) light of 254 nm. Obviously the PL emission intensity of Powder O is greatly reduced from that of Powder A. This quenching is caused by the partial oxidation of Ce^{3+} to Ce^{4+} after the reaction of the microspheres with the MnO_4^- oxidant in the aqueous solution. That is, the generation of Ce^{4+} in the $CePO_4$:Tb^{3+} phosphor promotes the intervalence $Ce^{3+} \rightarrow Ce^{4+}$ charge transfer and simultaneously disturbs the $Ce^{3+} \rightarrow Tb^{3+}$ energy transfer for the Tb^{3+} emission. In our previous work, the well-grown $CePO_4$:Tb^{3+} solid particles, which had the BET specific surface area as small as 1.3 $m^2\ g^{-1}$, by heating at a high temperature of 800 °C exhibited much less PL quenching after the similar oxidation treatment. The porous structure of the present microspheres is therefore effective for the detection of the oxidant in the solution due to the much larger amount of the surface reaction sites. The reduction of Powder O to R recovers the PL emission intensity, as seen in Fig. 8, although it does not reach the initial intensity of Powder

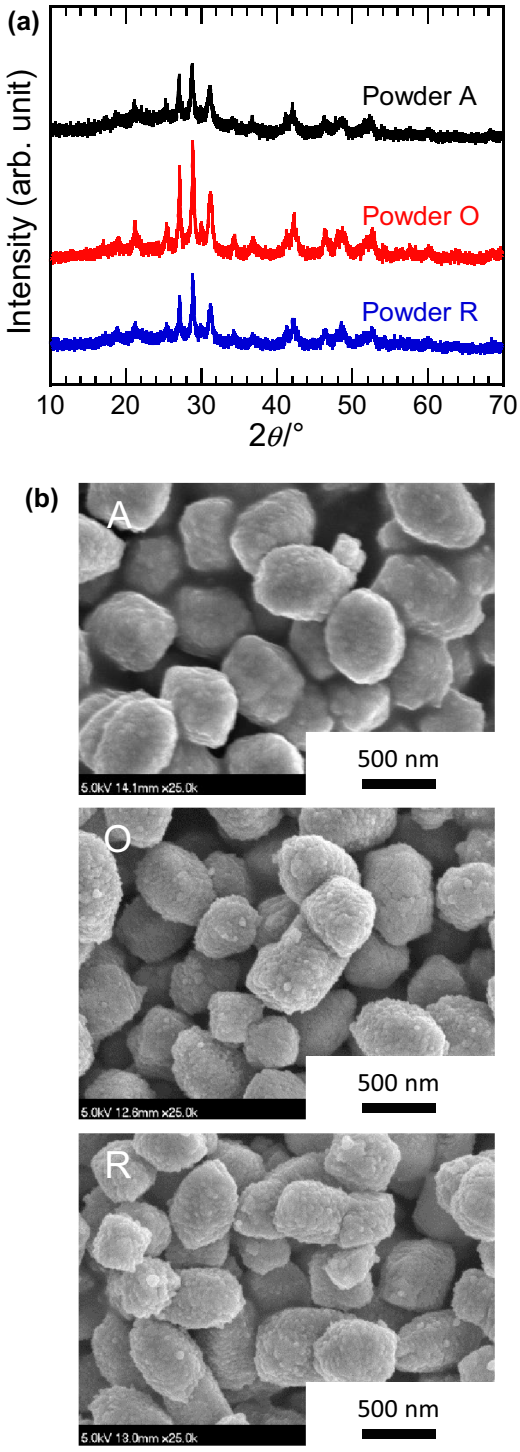

Fig. 7 **a** XRD patterns and **b** FESEM images of Powder A, the oxidized Powder O, and the oxidized/reduced Powder R

A. This may be related to the particle structure having the micropores. The inorganic MnO_4^- ion and the organic L(+)-ascorbic acid molecule differ in size and chemical nature, which would induce a difference in the rate of the penetration inside the microspheres.

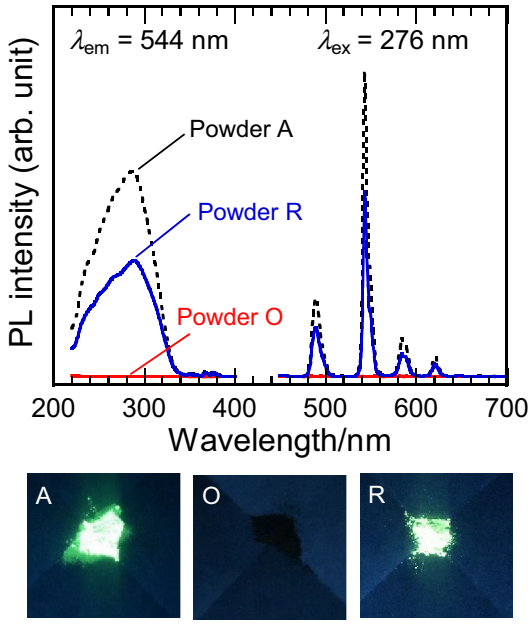

Fig. 8 PL excitation and emission spectra of Powder A, O, and R, together with their optical images under the irradiation of the 254-nm UV light

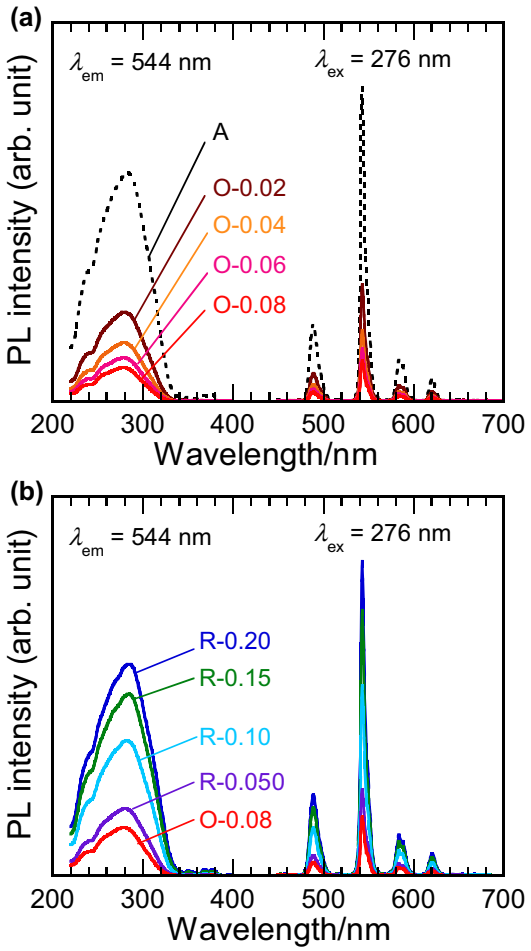

Fig. 9 PL excitation and emission spectra of **a** Powder O-*x* (*x* = 0.02, 0.04, 0.06, or 0.08) and **b** Powder R-*y* (*y* = 0.050, 0.10, 0.15, or 0.20)

Next, we examined the concentration dependence of the PL intensity for both the oxidant and the reductant in the redox treatment. The concentrations for this experiment were smaller than those employed in the above-mentioned redox treatment (Figs. 7, 8). Figure 9a shows PL excitation and emission spectra of Powder O-*x* (*x* = 0.02, 0.04, 0.06, or 0.08 in accordance with the $KMnO_4$ concentrations between 0.020 and 0.080 mmol L^{-1}), together with those of Powder A. After the oxidation treatment, the PL intensity of both the excitation and the emission decreases with the increase in the $KMnO_4$ concentration. This result indicates that the $CePO_4$:Tb^{3+} porous microspheres can be used for detecting quantitatively the oxidant in the aqueous solution. Powder O-0.08 was treated with the aqueous L(+)-ascorbic acid solutions with the concentrations between 0.050 and 0.20 mmol L^{-1} to obtain Powder R-*y* (*y* = 0.050, 0.10, 0.15, or 0.20). The PL intensity of both the excitation and the emission is recovered gradually with the increase in the L(+)-ascorbic acid concentration, as shown in Fig. 9b.

For the quantitative analysis of the redox response, the PL intensity of the Tb^{3+} emissions was integrated in the wavelength region between 470 and 640 nm. The integrated intensity (denoted as Φ) was then normalized by the initial value of Powder A (taken as $\Phi = 100\%$). In Fig. 10, Φ is plotted against the concentration of the $KMnO_4$ (C_{ox}) and the L(+)-ascorbic acid solution (C_{red}) for Powder O-*x* and Powder R-*y*, respectively. Φ decreases rapidly with the increase in C_{ox} for Powder O-*x* (Fig. 10a) and the plot is well fitted with an exponential function as follows.

$$\Phi = 79.3 \exp\left(-44.9 C_{ox}\right) + 11.0 \quad (2)$$

The exponential manner of the luminescence quenching by the oxidation is ascribed to the optical absorption due to the $Ce^{3+} \rightarrow Ce^{4+}$ charge transfer. Actually we reported the exponential function without a constant term, $\Phi = 96.6\exp(-17.6 C_{ox})$, in the case of the $CePO_4$:Tb^{3+} nanorod samples. The discrepancy arises from the structure of the phosphor particles. In the aggregated microspheres with the hierarchically porous structure, the $KMnO_4$ solution may not reach their central region, thereby preventing the quenching of the Tb^{3+} emissions. The residual luminescence would give the constant term in the Eq. (2).

For Powder R-*y*, Φ increases differently with the increase in C_{red} (Fig. 10b). At the low concentration, the plot is fitted with an exponential function as follows.

$$\Phi = 2.23 \exp\left(26.7 C_{red}\right) + 10.9 \quad (3)$$

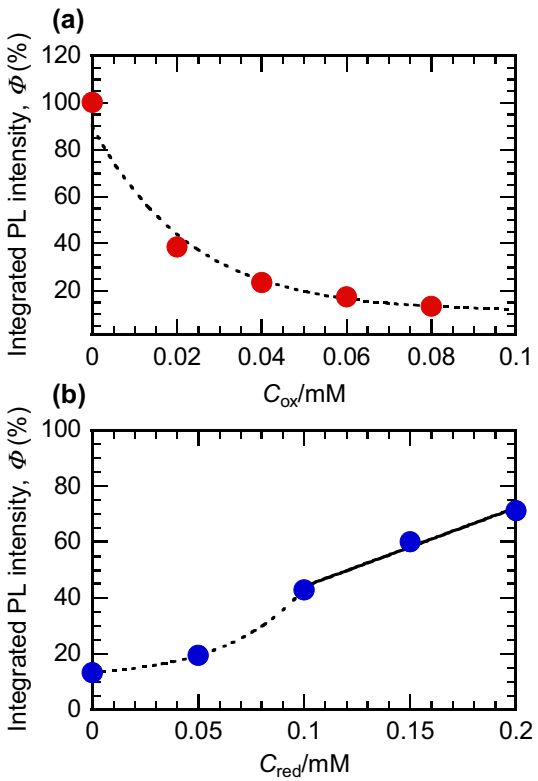

Fig. 10 Relationship between the integrated PL intensity (Φ) and the concentration of **a** the oxidant (C_{ox}) for Powder O-*x* and **b** the reductant (C_{red}) for Powder R-*y*

The constant term is almost the same as that of the Eq. (2). At the high concentration, the plot is changed to a linear function expressed as follows.

$$\Phi = 282C_{red} + 15.7 \quad (4)$$

The appearance of the two functions is explained based on the particle structure. While the primary nanoparticles near the outer surface of the microspheres are easily reduced like the nanorod samples, those in the central region are difficult to be reduced due to the extended diffusion path and time of the L(+)-ascorbic acid molecules. Therefore, at the low concentration, most of the reductants are consumed at the surface and the central region remains unreduced. At the high concentration, the primary nanoparticles near the surface are fully reduced and those in the central region are gradually reduced by the diffusing reductants. Anyway, the plots in Fig. 10 can be used as calibration curves for sensing of redox species through luminescence quenching and recovery of the $CePO_4$:Tb^{3+} microspheres, which are easy to handle in the field as well as in the laboratory. In that case, because the redox response of the $CePO_4$:Tb^{3+} materials depends largely on the reaction temperature and time (the response is generally better at higher temperatures or for longer time) [8, 9], the calibration curves should be made in accordance with the respective redox conditions.

As to the stability of the $CePO_4$:Tb^{3+} materials, we have already shown that $CePO_4$:Tb^{3+} can be used with at least four cycles of the redox treatments [9]. These treatments were carried out with much higher concentrations of the redox reagents (5 mmol L^{-1}) at a higher temperature of 80 °C, as compared to the conditions employed in present study (up to 0.50 and 1.25 mmol L^{-1} for the oxidant and the reductant, respectively, at room temperature). This fundamental stability of the $CePO_4$:Tb^{3+} materials appears to be independent of their microstructures at least within our experimental conditions.

4 Conclusions

The $CePO_4$:Tb^{3+} porous microspheres, approximately 800 nm in size, were synthesized by the hydrothermal method assisted with EDTA. The microspheres actually consisted of primary nanoparticles and hence had a high specific surface area of 51.4 m^2 g^{-1}. The microspheres showed the green PL from the doped Tb^{3+} ions upon excitation of the Ce^{3+} ions by the UV light. With the redox treatment of the microspheres, the PL intensity was once decreased by the oxidation and then recovered by the reduction. The PL quenching behavior was explained with the formation of Ce^{4+} by the oxidation and the subsequent appearance of the Ce^{3+} to Ce^{4+} intervalence charge transfer state, which disturbed the Ce^{3+} to Tb^{3+} energy transfer. The redox sensitivity of the microspheres was further evaluated quantitatively against the concentrations of the oxidant and the reductant. The relationship between the integrated PL intensity and the oxidant or the reductant concentrations was approximated by the exponential or the linear function.

Acknowledgements This study was supported by JSPS KAKENHI (Grant No. 17K06801).

Compliance with ethical standards

Conflict of interest On behalf of all authors, the corresponding author states that there is no conflict of interest.

References

1. Blasse G, Grabmaier BC (1994) Luminescent materials. Springer, Berlin
2. Ozawa L (2007) Cathodoluminescence and photoluminescence: theories and practical applications. CRC Press, Boca Raton
3. Gan W, Xiao S, Gao L, Gao R, Li J, Zhan X (2017) Luminescent and transparent wood composites fabricated by poly(methyl

methacrylate) and γ-Fe_2O_3@YVO_4:Eu^{3+} Nanoparticle Impregnation. ACS Sustain Chem Eng 5:3855–3862
4. McKenna B, Evans RC (2017) Towards efficient spectral converters through materials design for luminescent solar devices. Adv Mater 29:1606491
5. McKittrick J, Shea-Rohwer LE (2014) Down conversion materials for solid-state lighting. J Am Ceram Soc 97:1327–1352
6. Feng W, Zhu X, Li F (2013) Recent advances in the optimization and functionalization of upconversion nanomaterials for in vivo bioapplications. NPG Asia Mater 5:e75
7. Tsuchiya Y, Hagiwara M, Fujihara S (2018) Fluorochromic properties of undoped and Ln^{3+}-doped $CaWO_4$ phosphor particles. ECS J Solid State Sci Technol 7:R50–R56
8. Kitsuda M, Fujihara S (2011) Quantitative luminescence switching in $CePO_4$:Tb by redox reactions. J Phys Chem C 115:8808–8815
9. Fujihara S, Takano Y, Kitsuda M (2015) Microstructural aspects of the $CePO_4$:Tb^{3+} phosphor for luminescence sensing. Int J Appl Ceram Technol 12:411–417
10. Lucas S, Champion E, Bernache-Assollant D, Leroy G (2004) Rare earth phosphate powders $RePO_4 \cdot nH_2O$ (Re = La, Ce or Y) II. Thermal behavior. J Solid State Chem 177:1312–1320
11. Clavier N, Podor R, Dacheux N (2011) Crystal chemistry of the monazite structure. J Eur Ceram Soc 31:941–976
12. Gulnar AK, Sudarsan V, Vatsa RK, Hubli RC, Gautam UK, Vinu A, Tyagi AK (2009) $CePO_4$:Ln (Ln = Tb^{3+} and Dy^{3+}) nanoleaves incorporated in silica sols. Cryst Growth Des 9:2451–2456
13. Gulnar AK, Sudarsan V, Vatsa RK, Sakuntala T, Tyagi AK, Gautam UK, Vinu A (2010) Nucleation sequence on the cation exchange process between $Y_{0.95}Eu_{0.05}PO_4$ and $CePO_4$ nanorods. Nanoscale 2:2847–2854
14. Masuda M, Hagiwara M, Fujihara S (2016) Room-temperature fabrication of nanocrystalline $CePO_4$:Tb^{3+} films by SILAR method and their luminescence-switching properties. J Ceram Soc Jpn 124:37–41
15. Wheelwright EJ, Spedding FH, Schwarzenbach G (1953) The stability of the rare earth complexes with ethylenediaminetetraacetic acid. J Am Chem Soc 75:4196–4201
16. Masui T, Tategaki H, Furukawa S, Imanaka N (2004) Synthesis and characterization of new environmentally-friendly pigments based on cerium phosphate. J Ceram Soc Jpn 112:646–649
17. Antony CJ, Aatiq A, Panicker CY, Bushiri MJ, Varghese HT, Manojkumar TK (2011) FT-IR and FT-Raman study of Nasicon type phosphates, $ASnFe(PO_4)_3$ [A = Na_2, Ca, Cd]. Spectrochim Acta A 78:415–419
18. Ekthammathat N, Thongtem T, Phuruangrat A, Thongtem S (2012) Facile hydrothermal synthesis and optical properties of monoclinic $CePO_4$ nanowires with high aspect ratio. J Nanomater 2012:958593
19. Deacon GB, Phillips RJ (1980) Relationships between the carbon-oxygen stretching frequencies of carboxylato complexes and the type of carboxylate coordination. Coord Chem Rev 33:227–250
20. Ryczkowski J (2000) FT-IR study of the adsorption of some complexones and of EDTA alkaline salts into alumina. Vib Spectrosc 22:55–62
21. Li C, Wang G, Evans DG, Duan X (2004) Incorporation of rare-earth ions in Mg–Al layered double hydroxides: intercalation with an [Eu (EDTA)]−chelate. J Solid State Chem 177:4569–4575
22. Kumar AS, Indrasenan P (2008) Thermal decomposition studies of lanthanide (III) complexes of EDTA. Asian J Chem 20:5178–5186
23. Sing KSW, Everett DH, Haul RAW, Moscou L, Pierotti RA, Rouquérol J, Siemieniewska T (1985) Reporting physisorption data for gas/solid systems with special reference to the determination of surface area and porosity. Pure Appl Chem 57:603–619
24. Yu J, Wang G, Cheng B, Zhou M (2007) Effects of hydrothermal temperature and time on the photocatalytic activity and microstructures of bimodal mesoporous TiO_2 powders. Appl Catal B 69:171–180